ELSEVIER

Journal of Biomechanics ▮ (▮▮▮▮) ▮▮▮–▮▮▮

JOURNAL OF BIOMECHANICS

www.elsevier.com/locate/jbiomech
www.JBiomech.com

Structural and nanoindentation studies of stem cell-based tissue-engineered bone

Gadi Pelled[a,1], Kuangshin Tai[b,1], Dima Sheyn[a], Yoram Zilberman[a], Sangamesh Kumbar[c], Lakshmi S. Nair[c], Cato T. Laurencin[c], Dan Gazit[a], Christine Ortiz[b,*]

[a]*Skeletal Biotech Laboratory, Hebrew University, Hadassah Medical Center, Ein Kerem, Jerusalem 91120, Israel*
[b]*Department of Materials Science and Engineering, Massachusetts Institute of Technology, 77 Massachusetts Avenue, Cambridge, MA 02139, USA*
[c]*Department of Orthopaedic Surgery, University of Virginia, Charlottesville, VA 22903, USA*

Accepted 15 December 2005

Abstract

Stem cell-based gene therapy and tissue engineering have been shown to be an efficient method for the regeneration of critical-sized bone defects. Despite being an area of active research over the last decade, no knowledge of the intrinsic ultrastructural and nanomechanical properties of such bone tissue exists. In this study, we report the nanomechanical properties of engineered bone tissue derived from genetically modified mesenchymal stem cells (MSCs) overexpressing the rhBMP2 gene, grown in vivo in the thigh muscle of immunocompetent mice for 4 weeks, compared to femoral bone adjacent to the transplantation site. The two types of bone had similar mineral contents (61 and 65 wt% for engineered and femoral bone, respectively), overall microstructures showing lacunae and canaliculi (both measured by back-scattered electron microscopy), chemical compositions (measured by energy dispersive X-ray analysis), and nanoscale topographical morphologies (measured by tapping-mode atomic force microscopy imaging or TMAFM). Nanoindentation experiments revealed that the small length scale mechanical properties were statistically different with the femoral bone (indented parallel to the bone long axis) being stiffer and harder (apparent elastic modulus, $E \sim 27.3 \pm 10.5$ GPa and hardness, $H \sim 1.0 \pm 0.7$ GPa) than the genetically engineered bone ($E \sim 19.8 \pm 5.6$ GPa, $H \sim 0.9 \pm 0.4$ GPa). TMAFM imaging showed clear residual indents characteristic of viscoelastic plastic deformation for both types of bone. However, fine differences in the residual indent area (smaller for the engineered bone), pile up (smaller for the engineered bone), and fracture mechanisms (microcracks for the engineered bone) were observed with the genetically engineered bone behaving more brittle than the femoral control.

Keywords: Gene therapy; Tissue engineering; Atomic force microscopy; Stem cells; Nanoindentation; Nanomechanics

1. Introduction

Bone regeneration presents a major challenge to orthopedic medicine. Current methods of treating massive bone loss mainly depend on artificial prostheses, which fail in the long term and often result in the loss of function and morbidity. Mesenchymal stem cell (MSC)-based tissue engineering has been reported to be an innovative and efficient approach for regenerating bone tissue in vivo (Hasharoni et al., 2005; Moutsatsos et al., 2001). The expression of an osteogenic growth factor from the BMP family (e.g., BMP-2, BMP-6, BMP-9) by MSCs exerts a paracrine effect on the host MSCs and an autocrine effect on the engineered MSCs (Gazit et al., 1999; Li et al., 2002). Thus, enhanced bone formation is achieved by both the host MSCs and the engrafted engineered MSCs. In spite of the extensive research

*Corresponding author. Tel.: +1 617 452 3084.
fax: +1 617 258 6936.
E-mail address: cortiz@mit.edu (C. Ortiz).
[1]Equally contributed to this work.

0021-9290/$ - see front matter © 2006 Elsevier Ltd. All rights reserved.
doi:10.1016/j.jbiomech.2005.12.012

performed on genetically engineered stem cell-based bone tissue engineering during the last decade, no knowledge of the intrinsic ultrastructural and nanomechanical properties of such bone tissue exists. In order for this approach to be optimized for clinical settings, a thorough multiscale analysis of the chemical and physical properties needs to be systematically carried out.

New nanoscale methodologies, applied in particular to bone, such as atomic force microscopy imaging (Tai et al., 2005; Hassenkam et al., 2004; Fantner et al., 2004, 2005; Xu et al., 2003), high resolution force spectroscopy (Thompson et al., 2001; Currey, 2001; Fantner et al., 2005), and nanoindentation (Tai et al., 2005; Rho and Pharr, 2000; Thompson et al., 2001; Ferguson et al., 2003; Hengsberger et al., 2001) enable a window into the fine details of structure and mechanical behavior at extremely small length scales. In some cases, micro and macroscopic assays, which yield averaged quantities over larger length scales, may not be sensitive enough to identify the underlying differences between two different sample populations and hence, nanoscale studies are desirable. In addition, nanoscale methodologies are useful when the volume of material available is too small for larger scale analyses, for example with tissue-engineered bone formation in critical-sized defects and mouse models. The accuracy of biomechanical properties reduced using traditional engineering beam theory applied to whole bone bending tests on mouse bone has also been questioned (Silva et al., 2004). Nanoindentation studies, in particular, have focused on differences between cortical and trabecular bone (Rho et al.,1997), variations as a function of distance from the osteonal center (Hengsberger et al., 2001) through the femoral cortex (Rho et al., 1999), anisotropy (Fan et al., 2002), viscoelasticity and time-dependent plasticity (Fan and Rho, 2003), and variations due to mineral content (Tai et al., 2005; Ferguson et al., 2003). Other mineralized biological materials such as dentin (Marshall et al., 2001b), enamel (Marshall et al., 2001a), and calcified cartilage (Ferguson et al., 2003) have also been studied using this technique. Recent clinically relevant studies include nanoindentation properties of aged bones (Nalla et al., 2005; Kavukcuoglu et al., 2005; Rho et al., 2002), the senescence-accelerated mouse as a model for senile osteoporosis (Silva et al., 2004; Malzbender, 2005), and rat osteopetrotic mutations (Jamsa et al., 2002).

Here we report, for the first time, a comparison of the nanoindentation properties and nanoscale deformation mechanisms of tissue-engineered bone derived from genetically engineered MSCs that were implanted ectopically in mice in vivo to native femoral bone adjacent to the implantation site. Other supplementary techniques were employed to further interpret the nanoscale data including back-scattered electron microscopy (BSEM) to estimate mineral content, Raman spectroscopy to identify chemical bonds, energy-dispersive X-ray (EDX) analyses for elemental analysis, histology, and microcomputerized tomography (μCT) scans for morphology and quantitative analysis. Such multitechnique investigations that combine new nanotechnological methodologies with traditional characterization tools will be crucial for the advancement of gene therapy and tissue engineering platforms towards the clinical settings.

2. Materials and methods

2.1. Genetically engineered MSCs expressing rhBMP-2

As described previously (Moutsatsos et al., 2001), cells from the C3H10T1/2 MSC line were stably transfected with a ptTATop-BMP2 plasmid vector that encodes for both a tetracycline transactivator and rhBMP-2 (tet-off system). The inducible human BMP-2 expression vector, ptTATop-BMP2, has a bidirectional promoter (TATA sequence) and consists of six tetracycline operators flanked by two transcriptional units with opposite orientations. In this vector, the level of the transactivator, which activates the bidirectional promoter, as well as the expression of hBMP-2 can be regulated by doxycycline, an analogue of tetracycline, yielding higher levels of gene expression as well as a greater frequency of inducible clones. The engineered MSCs were grown in DMEM supplemented with 2 mM L-glutamine, 100 units/ml penicillin, 100 units/ml streptomycin, and 10%FCS (Biological Industries, Kibbutz Beit Haemek, Israel). Doxycycline was supplemented to the culture media in order to prevent cell differentiation before implantation.

2.2. In vivo ectopic bone formation

After trypsinization, aliquots of $\sim 3 \times 10^6$ BMP2-expressing MSCs were seeded onto pre-cut, electrospun poly(lactide-co-glycolide) fiber mats (3 mm × 3 mm, fiber diameters ~4–8 μm) (Li et al., 2002). Prior to transplantation, C3H/HeN female mice aged 6–8 weeks ($n = 10$) were anesthetized using ketamine–xylazine mixture, injected intra-peritoneally, and the thigh muscle skin was swabbed with isopropyl alcohol (70%) and chlorhexidine gluconate (0.5%). The skin and muscle were cut and the cell-seeded scaffolds were transplanted. Ectopic bone formation was monitored using in vivo fluoroscopy (Premier Encore Fluoroscan, Hologic, MA, USA) once in 2 weeks. Doxycycline was not supplemented to the mice drinking water in order to induce BMP-2 expression, which would lead to bone formation. About 4 weeks post transplantation, the mice were sacrificed.

2.3. Micro-computerized tomography (μCT)

Bone tissue was segmented from marrow and soft tissue using a global thresholding procedure. μCT (micro-CT40, Scanco, Switzerland) was carried out at a resolution of 20 μm. In addition to the visual assessment of structural images, morphometric indices were determined from the microtomographic datasets using direct 3D morphometry (Muller and Ruegsegger, 1997; Hildebrand et al., 1999). The ectopic bone volume was computed by contouring and the bone density was calculated according to the ratio of bone volume to total tissue volume.

2.4. Bone sample preparation

Samples were dissected from the sacrificed animals, rinsed with phosphate-buffered saline (PBS), and embedded in glycol methacrylate (JB-4 embedding kit, Electron Microscopy Sciences, PA, USA) in vacuum. Blocks were cut with a diamond-impregnated saw (Buehler) and then polished on Al_2O_3 paper (South Bay Technologies, 9–0.05 μm grit sizes). For histology only, samples were fixed in buffered formalin (4%, 24 h), decalcified in ethylenediamine tetraacetic acid (0.5 M, 3 weeks), passed through ethanol grade, and embedded in paraffin. Paraffin blocks were sectioned (5 μm thick) using a Leica RM2165 microtome (Germany) and stained using hematoxilin–eosin(H&E) and Masson's Trichrome.

2.5. BSEM, Raman spectroscopy, and EDX

A low vacuum electron detection ESEM (Philips/FEI XL30 FEG-SEM, Hillsboro, OR, USA) was employed in back-scattered mode in a water vapor environment to image uncoated samples. Mineral contents were calculated from grayscale pixel values which directly correlate with average atomic number and mineral content (Skedros et al., 1993a,b). Raman spectroscopy was carried out with a Kaiser Hololab 5000R (Ann Arbor, MI, USA). EDX was carried out with a sapphire detector (EDAX, Mahwah, NJ, USA).

2.6. Nanoindentation

Load-controlled nanoindentation experiments were conducted in ambient conditions using a Hysitron Inc. (Minneapolis, MN, USA) Triboindenter and a Berkovich diamond probe as previously reported (Tai et al., 2005). Each experiment involved a four-segment load function: a 3 s hold at zero load; a constant loading rate of 50 μN/s until the maximum set peak load was reached; a hold of 20 s; and finally a constant unloading rate of 50 μN/s. Three different maximum loads were applied at 500, 1000, and 7000 μN. Elastic moduli were calculated from the top 95–20% of the initial unloading curve by fitting these data to contact mechanical theory for an isotropic, elastic half-space (O–P method (Oliver and Pharr, 1992)).[2] Hardness (H = maximum load/area at maximum load) values were calculated from both the O–P contact area at maximum load and from contact areas measured by AFM imaging of residual indents immediately after indentation[3] (taken within a 20 min time period after indentation (Quesant Q-Scope350) in tapping mode (Tai et al., 2005)). Tests were conducted parallel to the long bone axis for the femoral bone and in the cortical-like surface region for the engineered bone. Six animals were tested. For each animal, both engineered bone and a corresponding femoral control pair were tested, each with >60 indents per maximum load where the indents were spaced 7 μm apart creating a 60 μm × 60 μm grid (constituting ~40% of the femur cross-section which was 150 μm). The total number of indents taken in this study was ~2160.

2.7. Statistical analysis

For nanoindentation data, a 3-way ANOVA statistical analysis as performed using Systat software (Point Richmond, CA, USA) taking into account the different types of bone (femoral versus engineered), the six different animals, and the three different maximum loads. For all other structural parameters, unpaired student t-tests were conducted on pooled datasets.

3. Results

3.1. μCT analysis

μCT scans (Fig. 1) indicate significant growth of ectopic bone in between the femur and tibia at the transplantation site. Quantitative analysis performed on the scanned engineered bone tissue indicated that the average bone volume reached 21.84 ± 2.61 SE mm^3

[2]It is important to note that indentation moduli reported here as estimated by the O–P method should be regarded as "apparent" or "effective" since this model neglects plasticity, viscoelasticity, pileup, and anisotropy (Oliver and Pharr, 2004) and the fact that they are known to vary with length scale (Malzbender, 2005). Recently, more advanced theoretical approaches have started to be developed which are continuum mechanical in nature, such as anisotropic elastic and elastic-perfectly plastic finite element analysis (Fan et al., 2004; Tai et al., 2005), poro-micromechanical models (Hellmich and Ulm, 2005), and two-phase composite formulations (Oyen and Ko, 2005). For the purposes of this paper, i.e. to compare an experimental model and a control, the O–P method is sufficient (Tai et al., 2005) and also has the advantage of enabling the analysis of a larger amount of data to get a more accurate statistical distribution in a reasonable period of time.

[3]The hardness calculated by the O–P method represents resistance to total deformation (elastic, viscoelastic, plastic) while the AFM-calculated hardness represents resistance to plasticity. The O–P hardness has a tendency to underestimate the contact area, hence overestimate the hardness (Oliver and Pharr, 2004).

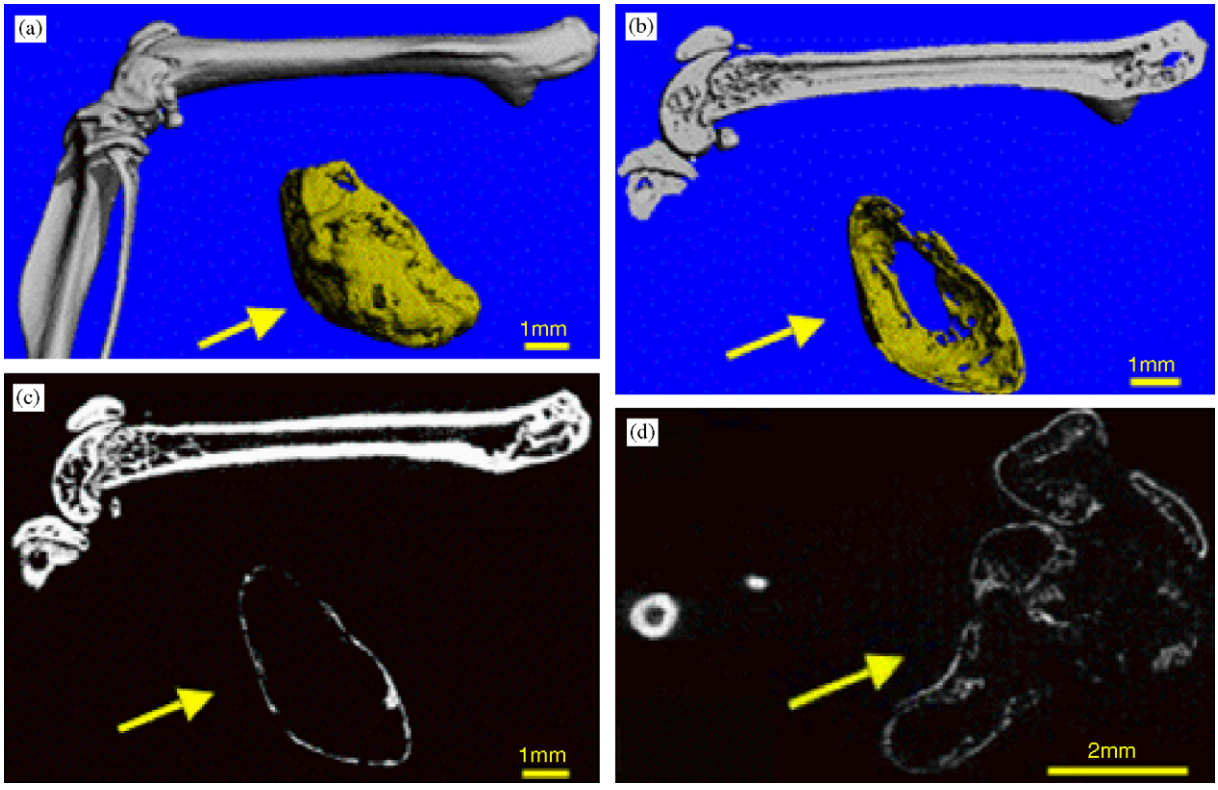

Fig. 1. 3D (a and b) and 2D (c and d) μCT images of femoral and genetically engineered bone (the latter indicated by arrows). Images obtained by μCT demonstrated the formation of new bone tissue within the implantation site. The new tissue had an outer cortical-like surface (c) and an inner compartment showing cancellous-like features (d). The outer (a) and inner (b—mid section) surface of the cortical-like region can be visualized using a 3D reconstruction of the μCT scans. All implants formed an oval-shaped structure following the initial 3D structure of the scaffold on which the cells had been seeded prior to implantation.

($n = 6$). The bone density was calculated to be 0.19 ± 0.0051 SE ($n = 6$). 2D images demonstrate that the new bone tissue is composed of distinct compact-like (Fig. 1c) and trabecular-like regions (Fig. 1d), as indicated by the degree of porosity on the outer and the inner regions, respectively. The outer and inner surfaces of the cortical-like region can be visualized using 3D reconstruction images (Fig. 1). These images highlight the powerful osteogenic potential of genetically engineered MSCs, which can induce robust bone formation within a short period of time.

3.2. Histological analysis

H&E staining of 5 μm sections of the newly formed engineered bone 4 weeks post implantation validated the results obtained by μCT scans (Fig. 2). A dense region of bone was seen at the outer aspect of the implant resembling compact bone. In the inner compartment of the implants more sparse bone trabecules were evident (Fig. 2b–d) surrounded by bone marrow. Thus, the inner compartment showed resemblance to native trabecular bone tissue. The presence of collagen within the new engineered bone trabecules was further demonstrated by a positive Masson's Trichrome staining (Fig. 2e, f).

3.3. Surface morphology and topography

BSEM of the femoral cortical bone (Fig. 3a, view down the long axis) shows a homogeneously mineralized structure (as reflected by the image grayscale) with uniformly shaped and oriented lacunae (elongated pores; average aspect ratio $= 3.4 \pm 1.0$, and average maximum dimension $= 9 \pm 2\,\mu m$) and canaliculi (channels emanating from lacunae). Osteons were not observed since mouse cortical bone does not undergo Haversian remodeling in the same manner as larger animals (Bianco and Robey, 2000). The genetically engineered bone (Fig. 3b) shows a similar degree and uniformity of mineralization as the femoral bone, but with larger lacunae that are more non-uniform in orientation and shape. The average aspect ratio and maximum dimension were 2.4 ± 1.0 and $13 \pm 5\mu m$, respectively ($p < 0.01$). Canaliculi were also observed. The femoral bone and engineered bone samples were found to exhibit ~5% and ~10% porosity, respectively, as calculated from the visible lacunae. The distributions of weight percent mineral content were statistically similar ($p < 0.001$) for genetically engineered (61.2 ± 3.3 wt%) and femoral bone (64.6 ± 2.0 wt.%). Smaller scan size BSEM images (Fig. 4) reveal similar smaller length scale nanostructures for both the femoral and engineered bone.

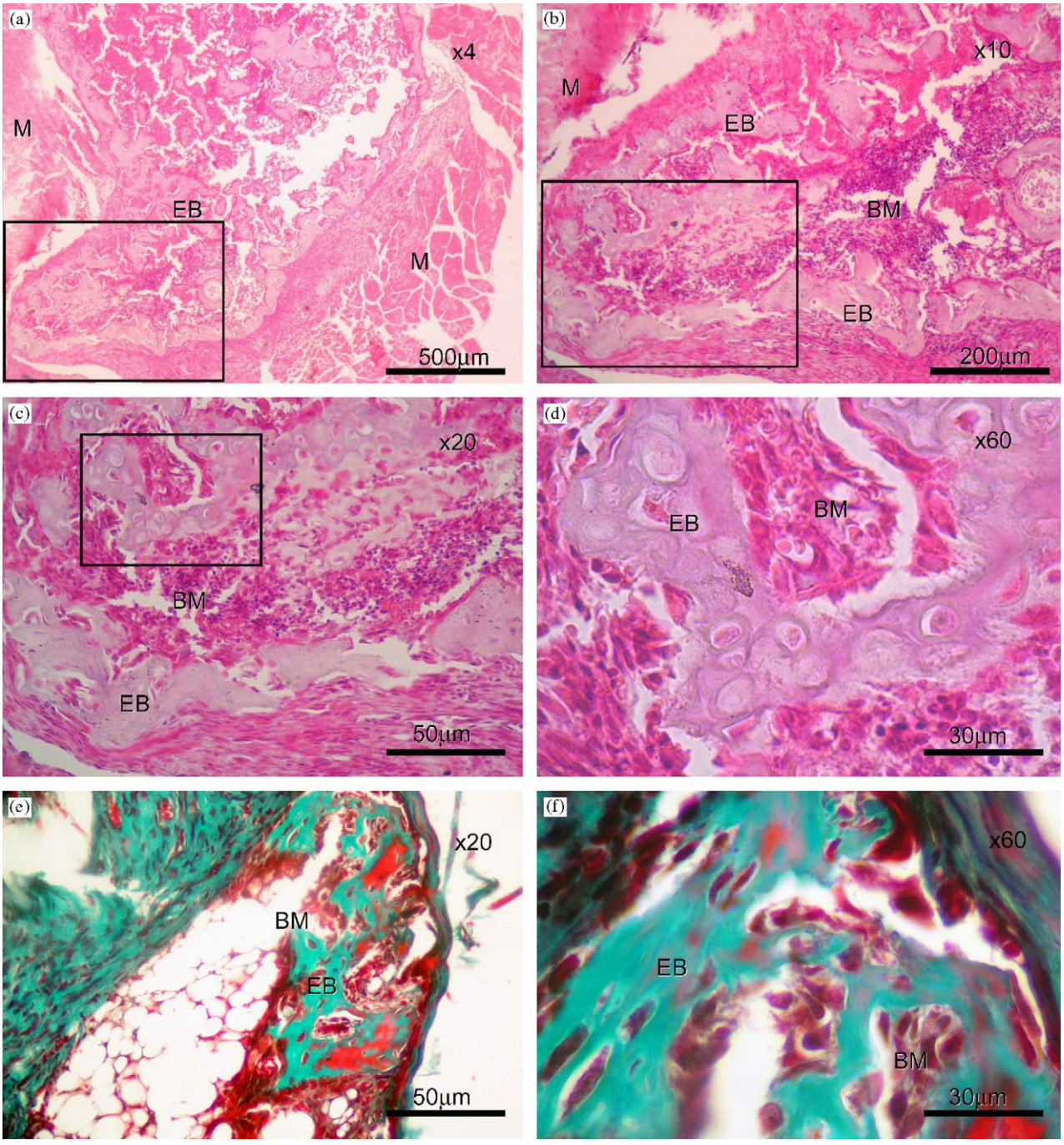

Fig. 2. Histological evaluation of the genetically engineered bone. Following μCT scans; bone samples were fixed in formalin and processed for histology. Hematoxilin–Eosin staining of 5 μm paraffin sections demonstrated the formation of an outer region of dense bone tissue, surrounding an inner compartment containing a cancellous-like inner portion (a). Higher magnifications showed the presence of bone marrow within in the new bone (b, c, d). Masson's Trichrome staining indicated that the engineered bone was composed of collagen stained with green color (e, f). EB = engineered bone; M = muscle; BM = bone marrow (b is a 10 × magnification of the inlet in a; c is the magnification of the inlet in b; d is the magnification of the inlet in c).

3.4. Chemical analysis

Raman spectra for the femoral and engineered bone showed similar structural compositions (Fig. 5) and peaks characteristic of the mineral and organic phases. There was an observed increase in intensity for the amide I band in the engineered bone as compared to the femoral bone. EDX indicates elemental composition and relative mineral content proportions in both types of bone to be similar as well (Fig. 6). The Ca/P ratios for the femoral and engineered bone were found to be 0.77 and 0.70, respectively.

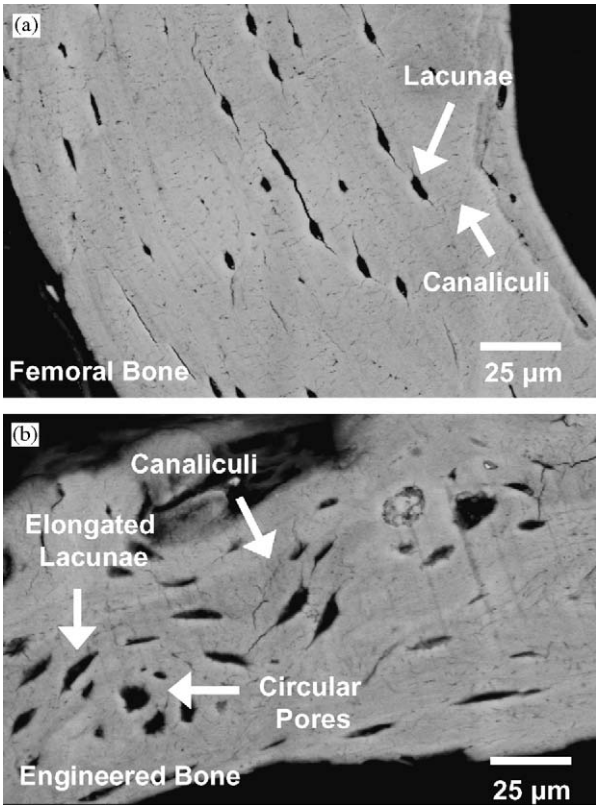

Fig. 3. Environmental back-scattered scanning electron microscope images at 500× magnification of (a) femoral (~1/10 of the entire femoral cross-section) and (b) genetically engineered bone. The femoral view orientation is along the long bone axis and the genetically engineered bone is the outer cortical-like surface. Closer inspection reveals the presence of channels emanating from the lacunae (a), which are presumably canaliculi. BSEM images of the cortical-like outer shell of the genetically engineered bone (b) shows a similar degree and uniformity of mineralization as the femoral bone, but with larger pores that are more non-uniform in orientation and shape. It this section, we observe two larger, more circular pores surrounded circumferentially by elongated pores in the central portion of the section, and elongated pores with their long axes aligned parallel to the outer edge of the section. Canaliculi are also observed. Imaging parameters were as follows: electron acceleration = 15 kV, operating current = 180 μA, working distance = 10.0 mm, water vapor = 0.3 Torr. This technique has a depth resolution of ~3 μm and a spatial resolution of ~10 μm.

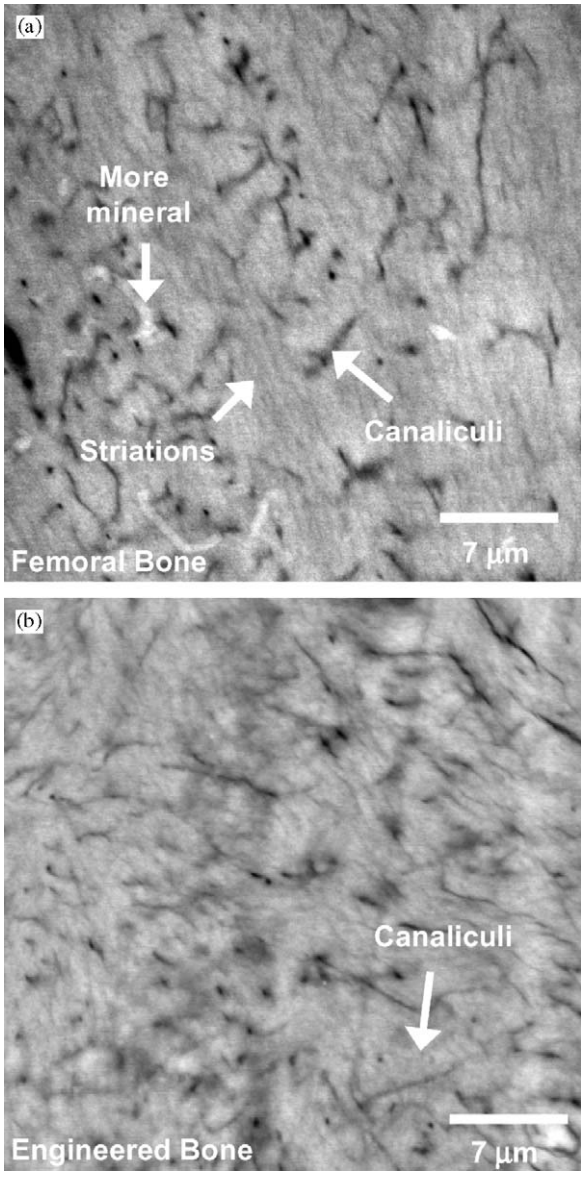

Fig. 4. Environmental back-scattered scanning electron microscope images at 2000× magnification of (a) femoral and (b) genetically engineered bone. The femoral view orientation is parallel to the long bone axis. Heterogeneities in mineral content are visible and darker streaks throughout, whose dimensions are consistent with canaliculi. The femoral bone appears to have small localized regions of high mineral content and oriented striations running throughout the entirety of the image. While some regions appeared anisotropic, completely oriented striations were not observed in the engineered bone. Imaging parameters were as follows: electron acceleration = 15 kV, operating current = 180 μA, working distance = 10.0 mm, water vapor = 0.3 Torr.

3.5. Nanoindentation

Force vs. indentation depth data for one pair of femoral and genetically engineered bone were averaged and plotted together (Figs. 7 and 8). Pooled data showed the genetically engineered bone (E~19.8±5.6 GPa, H~0.9±0.4 GPa) was less stiff and had a lower hardness than the femoral bone (E~27.3±10.5 GPa, H~1.0±0.7 GPa) ($n = 2449$, $p < 0.0005$), as calculated from the O–P method. Statistical differences between different animals as well as the three chosen maximum loads were observed for both elastic modulus and hardness values ($p < 0.0005$). In particular, the elastic modulus and hardness values were found to increase with decreasing maximum load. This is an expected result as the effects of underlying porosity and defects are lessened at smaller length scales. The distribution of calculated modulus and hardness values (Fig. 9) for both types of bone appear multimodal at lower maximum loads, and homogenized and narrow at higher maximum loads.

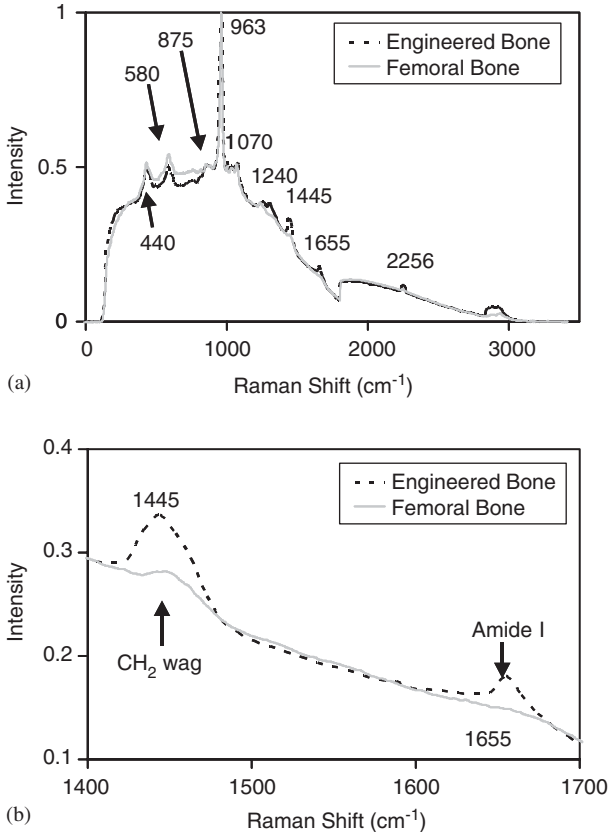

Fig. 5. Raman spectra for the femoral and genetically engineered bone (a) between 0 and 3500 cm^{-1} and (b) expanded region between 1400 and 1700 cm^{-1}. The notable peaks at 1080, 960, 595, and 435 cm^{-1} correspond to typical phosphate and carbonate bonding (Carden et al., 2003; Tarnowski et al., 2002) from the mineral phase. The most prominent peak at 960 cm^{-1} which corresponds to the phosphate ion P–O υ_1 symmetric stretch, is observed in both bone materials. (b) Peaks at 1445 and 1655 cm^{-1} specify the presence of a CH_2 wag and amide I bond, respectively, from the organic phase. Experiments were carried out at 785 nm utilizing coherent CW argon/ion and Ti/S lasers with a 100 μm diameter optical fiber to maximize throughput. This technique has a depth resolution ~1 μm and a spatial resolution ~50 μm.

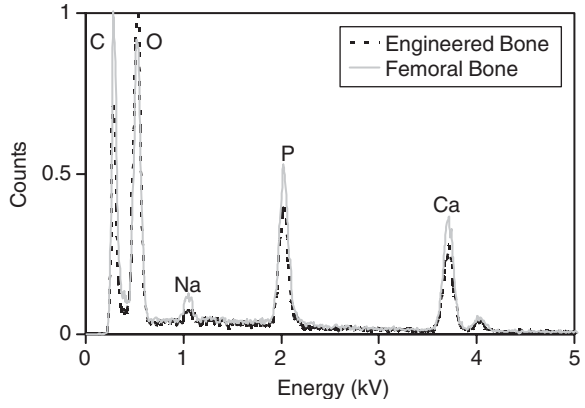

Fig. 6. Energy-dispersive X-ray spectra for both femoral and genetically engineered bone was carried out with a sapphire detector (EDAX, Mahwah, NJ, USA, depth resolution ~3 μm, spatial resolution ~10 μm).

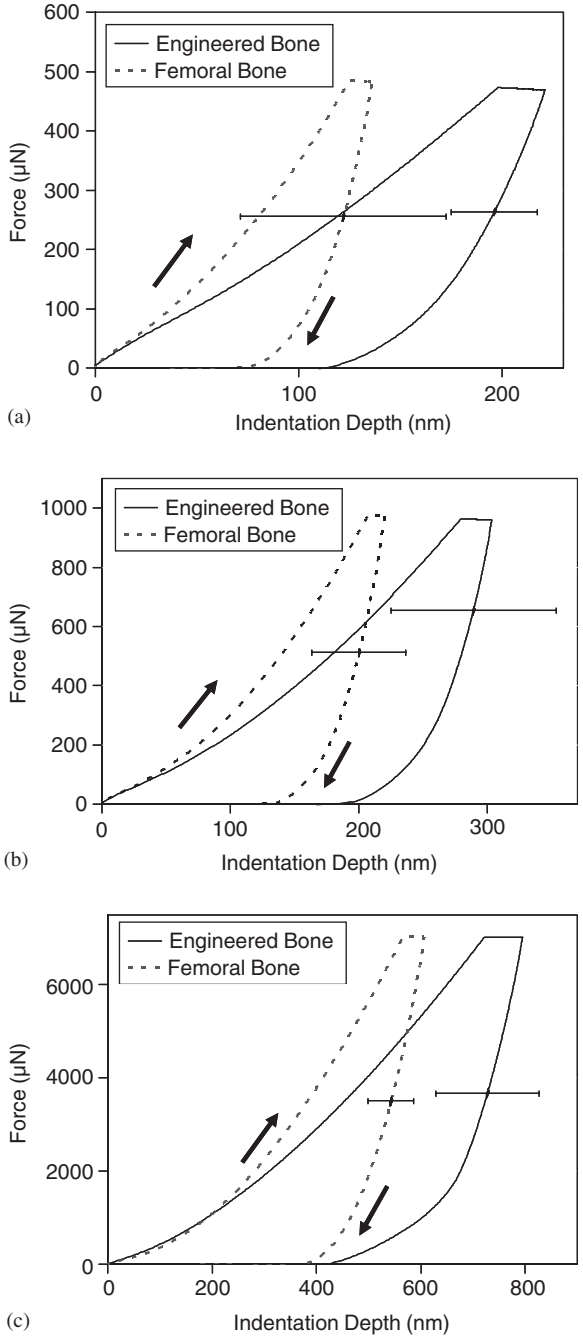

Fig. 7. Typical nanoindentaion data on loading and unloading using a Berkovich probe tip comparing femoral and genetically engineered bone from one particular mouse at maximum loads of (a) 500, (b) 1000, and (c) 7000 μN at a loading rate of 50 μN/s. There were >50 indents for each averaged curve where each indent was spaced 10 μm apart. The horizontal error bars represent ± standard deviation and are typical for the entire loading curve (i.e. vary by <5% with load). The femoral view orientation is parallel to the long bone axis and the genetically engineered bone is the outer cortical-like surface.

Hardness values calculated via AFM imaging of residual indents ($n = 12$) were similar to that calculated by the O–P method (0.7 ± 0.4 and 0.8 ± 0.4 for the femoral and engineered bone, respectively, $p > 0.01$). Although the

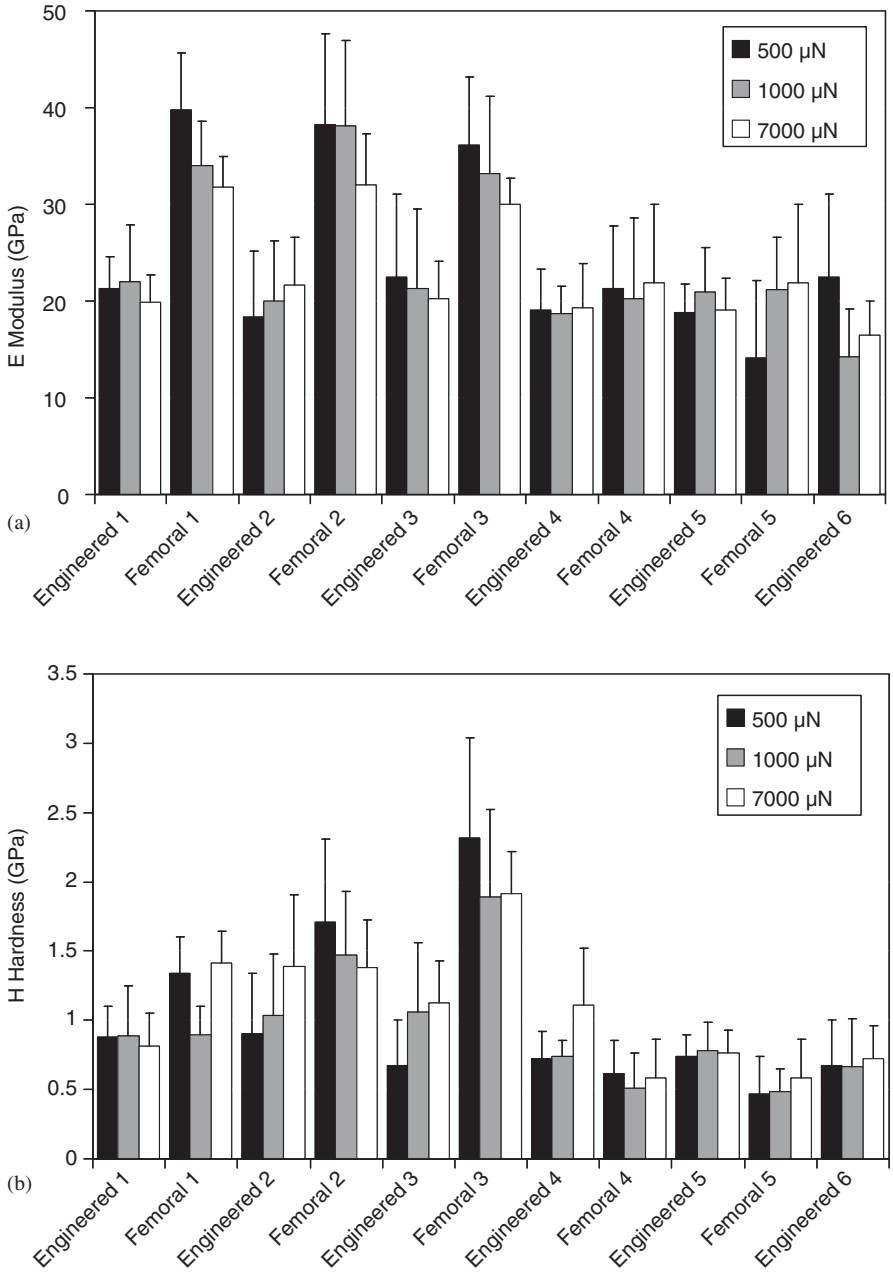

Fig. 8. Apparent (a) moduli and (b) hardnesses reduced from nanoindentation data via the Oliver–Pharr method (Oliver and Pharr, 1992) for six different bone sample pairs of mice (i.e. 6 different animals) at three different maximum loads with >50 indents for each set of data. The femoral view orientation is parallel to the long bone axis and the genetically engineered bone is the outer cortical-like surface. Hi-lo bars represent one standard deviation.

absolute values of hardness calculated via AFM are more accurate (since the residual indent area is directly measured), the O–P method enabled a much larger statistical dataset showing differences between the femoral and engineered samples.

3.6. Tapping-mode (TMAFM) imaging of residual indents

TMAFM images (Fig. 10) show clear viscoelastic plastic deformation (indicated by the residual indent impression) and an undeformed granular morphology away from the indent region for both samples. Flattening of these surface topographical features was observed within the indent region for both samples. The femoral bone exhibited pileup along the edges of the indent (~100 nm in height) while the genetically engineered bone did not (Fig. 10b,d). Along the edge of the engineered bone indent impression, microcracks were observed that were not apparent in the femoral bone (Fig. 10e, f). The average maximum lateral dimension of the topographical features away from the deformed

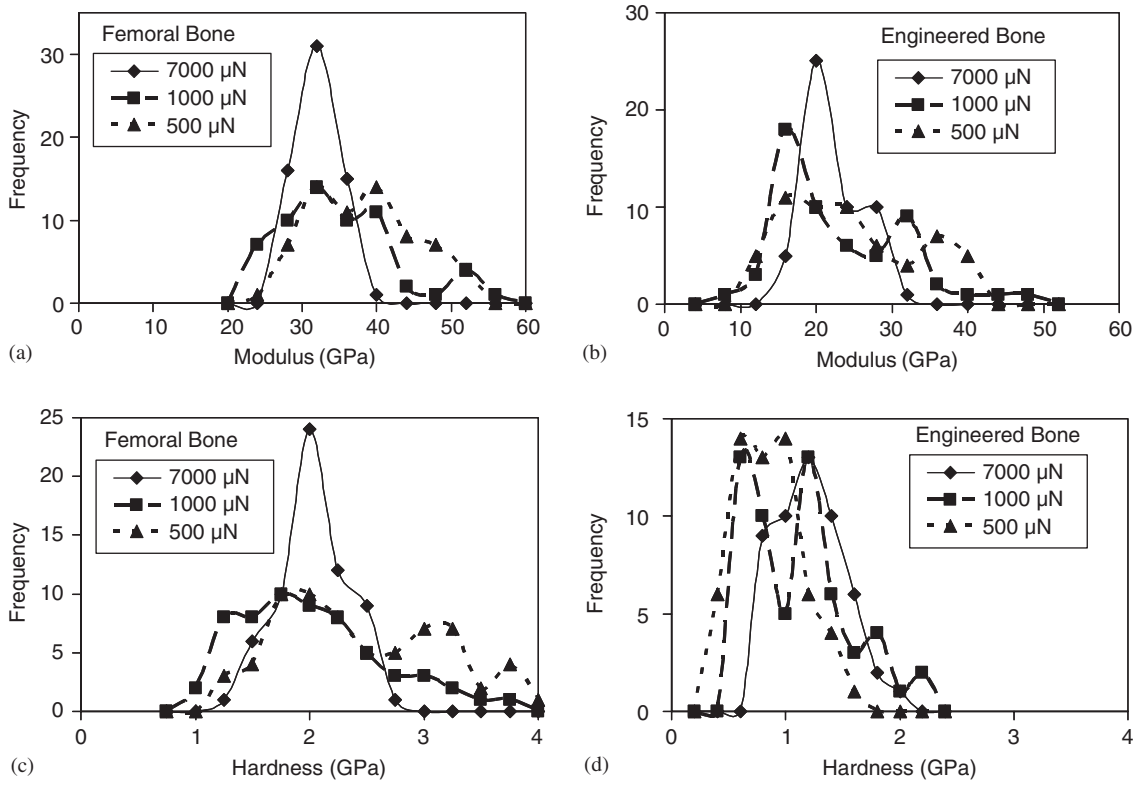

Fig. 9. Histograms of O–P calculated nanoindentation modulus and hardness values for femoral and engineered bone in animal 3 at the three different maximum loadings.

region for the femoral and engineered bone were 158 ± 80 and 145 ± 60 nm ($p < 0.05$). The peak-to-valley height values, for the femoral and engineered bone, were measured to be 34 ± 13 and 34 ± 15 nm, respectively ($p < 0.001$).

4. Discussion

Here we have shown that nanoindentation is a viable technique for quantifying the bio(nano)mechanical properties of small volumes of tissue-engineered bone produced in vivo, where larger scale mechanical testing methods was not possible. The averaged nanoindentation curves (Fig. 7) show a greater resistance to deformation in the femoral than the engineered bone as indicated by how far the indenter is able to penetrate the material for the same maximum force. Table 1 compares structural and nanomechanical data obtained from mice femoral and genetically engineered bone. While the two types of bone were found to have similar mineral contents, overall porous microstructures showing lacunae and canaliculi, chemical compositions, and nanoscale topographical morphologies, apparent elastic moduli reduced from nanoindentation data were found to be statistically different with the femoral bone (indented parallel to the bone long axis) being $\sim 1.4\times$ stiffer than the engineered bone. The average value obtained for the femoral bone (~ 27 GPa) is slightly lower than that reported in the literature (Silva et al., 2004; Kavukcuoglu et al., 2005) and may be due to the effects of alcohol and/or dehydration used in these studies (Rho and Pharr, 1999). O–P calculations showed that the femoral bone was $\sim 1.1\times$ harder than the engineered bone, and hence exhibited a greater resistance to total deformation (elastic, viscoelastic, and plastic). Since mineral content and nanoscale morphology were statistically similar for both types of bone, these parameters cannot be responsible for these material property trends. A Raman-suggested increase in collagen non-reducible pyridinoline crosslink content for the engineered bone (due to the increase in intensity for the amide I band (Nalla et al., 2005)) relative to the femoral would be expected to result in an increase in modulus and hence, cannot be responsible as well. Hence other origins could be as follows: (1) variations in the overall organization and interactions between the organic and mineral constituents; (2) variation in the composition and/or supramolecular structure of the organic component; and (3) differences in underlying porosity. Such structural variations could result from differences in age (i.e. the femoral bone is 10–12 weeks old and the ectopic is 4 weeks old) and/or loading conditions (i.e. the femoral bone is weight bearing while the ectopic is non-weight bearing). Ongoing nanotechnological studies provide a promising pathway to

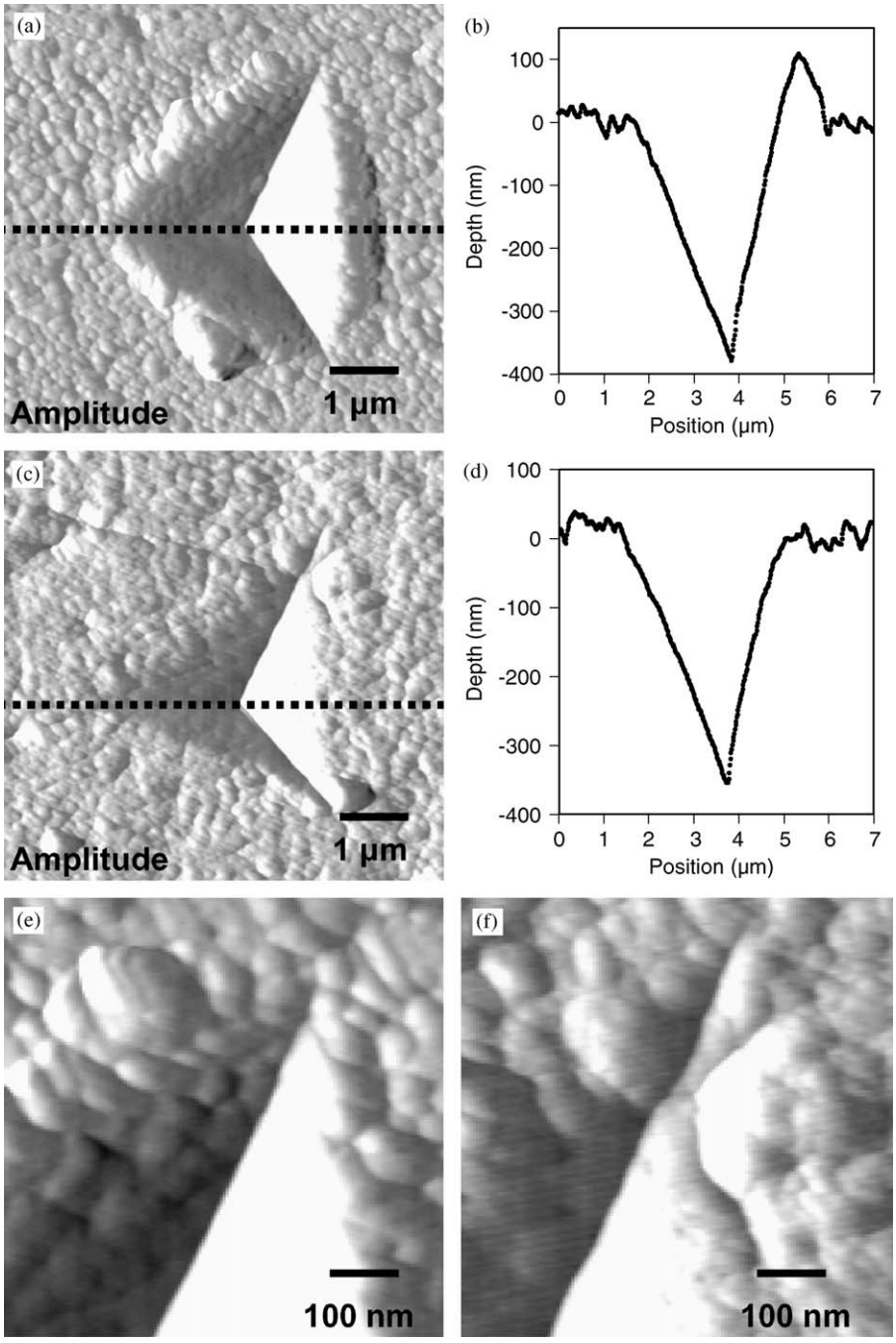

Fig. 10. TMAFM amplitude images and section profiles are given of the residual impressions after loading and unloading to 7000 μN using a Berkovich probe tip at a loading rate of 50 μN/s. The (a) femoral view orientation is parallel to the long bone axis and (b) the genetically engineered bone is the outer cortical-like surface. Amplitude images are reflective of abrupt surface topographical changes. Sectioned line scans through corresponding height images (not shown) show significant pileup for the (c) femoral bone, but a negligible amount for the (d) engineered bone. Signs of crack formation is not evident for the (e) femoral bone but is suggestive for the (f) engineered bone along the edge of the indent impression.

further investigate both of the above hypotheses, including; high-resolution tapping-mode AFM imaging as a function of acid demineralization (Tai et al., 2005) and chemically and spatially specific high-resolution force spectroscopy (Dean et al., 2005). Lastly, the engineered bone also exhibited a more heterogeneous distribution of material properties, which could be because of any of the three areas mentioned above.

Direct visualization of the nanoscale surface morphological features and deformation via in-situ high-resolution tapping-mode AFM imaging was achieved. The appearance and dimensions of the topographical

Table 1
Summary comparison of the structural and nanomechanical properties of femoral and genetically engineered bone

	Femoral	Engineered	*P*
Mineral content (BSEM, wt%)	64.6±2.0	61.2±3.2	>0.01
Lacunae aspect ratio (BSEM)	3.4±1.0	2.4±1.0	<0.01*
Lacunae maximum dimension (BSEM, μm)	9±2	13±5	<0.01*
Porosity (BSEM, %)	5	10	—
Ca/P Ratio (EDX)	0.77	0.70	—
Maximum dimension of topographical features (AFM, nm)	158±80	145±60	>0.01
Peak-to-valley height of topographical features (AFM, nm)	34±13	34±15	>0.01
O–P apparent nanoindentation moduli, *E* (GPa)	27.3±10.5	19.8±5.6	<0.0005*
O–P hardness, *H*, measured by nanoindentation (GPa)	1.0±0.7	0.9±0.4	<0.0005*
Hardness calculated from AFM residual indent (GPa)	0.7±0.3	0.8±0.4	>0.01

For O–P estimated elastic moduli and hardness values, a 3-way ANOVA statistical analysis as performed on 2449 indents which took into account the different types of bone (femoral versus engineered), the six different animals, and the maximum loads (500, 1000, and 7000 μN). All other statistical tests were unpaired student *t*-tests carried out on pooled datasets (* indicates a statistically significant difference between femoral and engineered bone samples).

features are slightly greater than that of previous studies of mineral particles in bone as determined by TMAFM (Eppell et al., 2001), SAXS (Fratzl et al., 1992) and X-ray diffraction (Landis, 1995; Biltz and Pellegrino, 1969; Mann, 2001; Wachtel and Weiner, 1994). This observation is likely due to assemblies of crystallites adhering together to form larger surface morphological features. Generally, both samples exhibited similar viscoelastic plastic deformation (i.e. a combination of viscoelastic and plastic behavior) at the length scales studied. However, fine differences in the residual indent area (smaller for the engineered bone), pile up (smaller for the engineered bone), and fracture mechanisms (microcracks for the engineered bone) were observed with the genetically engineered bone behaving more brittle than the femoral control. Viscoelastic plastic deformation at this length scale may arise from a variety of mechanisms including underlying porosity and voiding, which would relieve triaxial stresses, collagen fibril slippage (Sasaki and Odajima, 1996), collagen denaturation (Tai et al., 2005), debonding of mineral–organic interfaces (Kotha and Guzeslu, 2002), crosslink scission (Wang et al., 2002), crack formation and propagation (Tai et al., 2005), deformation and structural phase transformation (Vaidya et al., 1997), viscous stretching of the organic component (Thompson et al., 2001), and/or rupture of self-healing sacrificial bonds (Fantner et al., 2005). The origins of the time-dependent component in bone is largely considered to be due to the organic presence of macromolecular polymer chain stretching (Yamashita et al., 2002). Again, further nanomechanical studies will be able to shed insight into which deformation mechanisms may be dominant.

The relationship between nanoscale and macroscale mechanical properties and function is non-trivial as hierarchical structural effects undoubtedly play a significant role. Multiscale theoretical models have been reported that include tension–shear mineral strength optimization (Ji and Gao, 2004), mineral–organic interfacial shear strength (Kotha and Guzeslu, 2002), two-phase bone ultrastructural finite element modeling (Oyen and Ko, 2005), relative proportions of constituents in mineralized osteoid based on the generalized packing model (Lees, 1987), and scaled micromechanical models of a two-phase polycrystalline foam (Hellmich and Ulm, 2002). While theoretical approaches are still in early stages, their continued development and refinement depends critically on both a quantitative knowledge of the nanoscale material properties and a qualitative understanding of the nanoscale deformation mechanisms. Regarding genetically engineered bone, currently, the volume of material is too small for micro or macromechanical testing. While at this point nanomechanics alone cannot be employed to conclusively predict in vivo macroscopic function of genetically engineered tissue, it does provide additional critical information over larger scale characterization techniques and as shown in this paper, is able to discern differences between two sample populations that other structural techniques are not able to discern. Hence, currently nanomechanics can be used as an optimization tool for the assessment and development of improved regenerative therapies, for example via implanted cell number, transgene duration of expression, and scaffold design and composition. Future studies in this area include nanoindentation of the trabecular-like regions in the engineered bone, the rate dependence of nanoscale properties, the temporal evolution of bone remodeling, and the effects of mechanical loading of bone formation and adaptation, and at different implantation sites including critical-sized bone defects in flat and long bones. Such studies will be crucial to the advancement of the tissue engineering strategy towards human clinical trials.

Acknowledgments

The Whitaker Foundation and the US Army through the MIT Institute for Soldier Nanotechnologies (Contract no. DAAD-19-02-D0002) are thanked for funding.[4] The authors would also like to thank the MIT National Science Foundation Center for Materials Science and Engineering and Alan Schwartzmann and the MIT Department of Materials Science Nanomechanical Technological Laboratory for instrumentation training and usage, as well as Diana Chai for assistance with statistical analysis.

References

Bianco, P., Robey, P.G., 2000. Marrow stromal stem cells. Journal of Clinical Investigation 105, 1663–1668.

Biltz, R.M., Pellegrino, E.D., 1969. The chemical anatomy of bone I. A comparative study of bone composition in sixteen vertebrates. Journal of Bone and Joint Surgery 51-A, 456–466.

Carden, A., Rajachar, R.M., Morris, M.D., Kohn, D.H., 2003. Ultrastructural changes accompanying the mechanical deformation of bone. Calcified Tissue International 72, 166–175.

Currey, J.D., 2001. Biomaterials: Sacrificial bonds heal bone. Nature 414, 699.

Dean, D., Han, L., Grodzinsky, A.J., Ortiz, C., 2005. Compressive nanomechanics of opposing aggrecan macromolecules. Journal of Biomechanics, in press, doi:10.1016/j.jbiomech.2005.09.007.

Eppell, S.J., Tong, W., Katz, J.L., Kuhn, L., Glimcher, M.J., 2001. Shape and size of isolated bone mineralites measured using atomic force microscopy. Journal of Orthopaedic Research 19, 1027–1034.

Fan, Z., Rho, J.Y., 2003. Effects of viscoelasticity and time-dependent plasticity on nanoindentation measurements of human cortical bone. Journal of Biomedical Materials Research 67A, 208–214.

Fan, Z., Swadener, J.G., Rho, J.Y., Roy, M.E., Pharr, G.M., 2002. Anisotropic properties of human tibial cortical bone as measured by nanoindentation. Journal of Orthopaedic Research 20, 806–810.

Fan, Z., Rho, J.Y., Swadener, J.G., 2004. Three-dimensional finite element analysis of the effects of anisotropy on bone mechanical properties measured by nanoindentation. Journal of Materials Research 19, 114–123.

Fantner, G.E., Birkedal, H., Kindt, J.H., Hassenkam, T., Weaver, J.C., Cutroni, J.A., Bosma, B.L., Bawazer, L., Finch, M.M., Cidade, G.A.G., Morse, D.E., Stucky, G.D., Hansma, P.K., 2004. Influence of the degradation of the organic matrix on the microscopic fracture behavior of trabecular bone. Bone 35, 1013–1022.

Fantner, G.E., Hassenkam, T., Kindt, J.H., Weaver, J.C., Birkedal, H., Pechenik, L., Cutroni, J.A., Cidade, G.A.G., Stucky, G.D., Morse, D.E., Hansma, P.K., 2005. Sacrificial bonds and hidden length dissipate energy as mineralized fibrils separate during bone fracture. Nature Materials 4, 612–616.

Ferguson, V.L., Bushby, A.J., Boyde, A., 2003. Nanomechanical properties and mineral concentration in articular calcified cartilage and subchondral bone. Journal of Anatomy 203, 191–202.

Fratzl, P., Groschner, M., Vogl, G., Plenk, H.G., Eschberger, J., Fratxl-Zelman, N., Koller, K., Klaushofer, K., 1992. Mineral crystals in calcified tissues: A comparative study by SAXS. Journal of Bone and Mineral Research 7, 329–334.

[4]The content does not necessarily reflect the position of the government and no official endorsement should be inferred.

Gazit, D., Turgeman, G., Kelley, P., Wang, E., Jalenak, M., Zilberman, Y., Moutsatsos, I., 1999. Engineered pluripotent mesenchymal cells integrate and differentiate in regenerating bone: A novel cell mediated gene therapy. Journal of Gene Medicine 1, 121–133.

Hasharoni, A., Zilberman, Y., Turgeman, G., Helm, G.A., Liebergall, M., Gazit, D., 2005. Murine spinal fusion induced by engineered mesenchymal stem cells that conditionally express bone morphogenetic protein-2. Journal of Neurosurgery: Spine 3, 47–52.

Hassenkam, T., Fantner, G.E., Cutroni, J.A., Weaver, J.C., Morse, D.E., Hansma, P.K., 2004. High resolution AFM imaging of intact and fractured trabecular bone. Bone 35, 4–10.

Hellmich, C., Ulm, F.-J., 2002. Micromechanical model for ultrastructural stiffness of mineralized tissues. Journal of Engineering Mechanics 128, 898–908.

Hellmich, C., Ulm, J.F., 2005. Poro-micromechanics of bone: Impact loading and wave propagation. Materials Research Society Conference Proceedings 844, 255–561.

Hengsberger, S., Kulik, A., Zysset, P., 2001. A combined atomic force microscopy and nanoindentation technique to investigate the elastic properties of bone structural units. European Cells and Materials 1, 12–17.

Hildebrand, T., Laib, A., Muller, R., Dequeker, J., Ruegsegger, P., 1999. Direct 3-d morphometric analysis of human cancellous bone: microstructural data from spine, femur, iliac crest, and calcaneus. Journal of Bone and Mineral Research 14, 1167–1174.

Jamsa, T., Rho, J.Y., Fan, Z., MacKay, C.A., Marks, S.C., Tuukkanen, J., 2002. Mechanical properties in long bones of rat osteopetrotic mutations. Journal of Biomechanics 35, 161–165.

Ji, B., Gao, H., 2004. Mechanical properties of nanostructure of biological materials. Journal of the Mechanics and Physics of Solids 52, 1963–1990.

Kavukcuoglu, B., West, C., Denhardt, D.T., Mann, A.B., 2005. Effects of osteopontin deficiency and aging on nanomechanics of mouse bone. Materials Research Society Symposium Proceedings 844, 27–32.

Kotha, S.P., Guzeslu, N., 2002. Modeling the tensile mechanical behavior of bone along the longitudinal direction. Journal of Theoretical Biology 219, 269–279.

Landis, W.J., 1995. The strength of a calcified tissue depends in part on the molecular structure and organization of its constituent mineral crystals in their organic matrix. Bone 16, 533–544.

Lees, S., 1987. Considerations regarding the structure of the mammalian mineralized osteoid from viewpoint of the generalized packing model. Connective Tissue Research 16, 281–303.

Li, W.-J., Laurencin, C.T., Caterson, E.J., Tuan, R.S., Ko, F.K., 2002. Electrospun nanofibrous structure: a novel scaffold for tissue engineering. Journal of Biomedical Materials Research 60, 613–621.

Malzbender, J., 2005. Letter to the editor comment on "Nanoindentation and whole-bone bending estimates of material properties in bones from senescence accelerated mouse SAMP6". Journal of Biomechanics 38, 1191–1192.

Mann, S., 2001. Organic Matrix-Mediated Biomineralization. Biomineralization: Principles and Concepts in Bioinorganic Materials Chemistry. Oxford University Press, Oxford, UK, pp. 89–124.

Marshall, G.W., Balooch, M., Gallagher, R.R., Gansky, S.A., Marshall, S.J., 2001a. Mechanical properties of the dentinoenamel junction: AFM studies of nanohardness, elastic modulus, and fracture. Journal of Biomedical Materials Research 54, 87–95.

Marshall, G.W., Habelitz, S., Gallagher, R., Balooch, M., Balooch, G., Marshall, S.J., 2001b. Nanomechanical properties of hydrated carious human dentin. Journal of Dental Research 80, 1768–1771.

Moutsatsos, I.K., Turgeman, G., Zhou, S., Kurkalli, B.G., Pelled, G., Tzur, L., Kelley, P., Stumm, N., Mi, S., Muller, R., Zilberman, Y.,

Gazit, D., 2001. Exogenously regulated stem cell-mediated gene therapy for bone regeneration. Molecular Therapy 3, 449–461.

Muller, R., Ruegsegger, P., 1997. Micro-tomographic imaging for the nondestructive evaluation of trabecular bone architecture. Studies in Health Technology and Informatics 40, 61–79.

Nalla, R.K., Kruzic, J.J., Kinney, J.H., Balooch, M., Ager III, J.W., Martin, M.C., Tomsia, A.P., Ritchie, R.O., 2005. Effects of aging on the toughness of human cortical bone: A study from nano to macro size-scales. Materials Research Society Conference Proceedings 844, 53–58.

Oliver, W.C., Pharr, G.M., 1992. An improved technique for determining hardness and elastic modulus using load and displacement sensing indentation experiments. Journal of Materials Research 7, 1564–1583.

Oliver, W.C., Pharr, G.M., 2004. Measurement of hardness and elastic modulus by instrumented indentation: Advances in understanding and refinements to methodology. Journal of Materials Research 7, 1564–1583.

Oyen, M.L., Ko, C.C., 2005. Finite element modeling of bone ultrastructure as a two-phase composite. Materials Research Society Conference Proceedings 844, 263–268.

Rho, J.Y., Pharr, G.M., 1999. Effects of drying on the mechanical properties of bovine femur measured by nanoindentation. Journal of Materials Science—Materials in Medicine 10, 485–488.

Rho, J.Y., Pharr, G.M., 2000. Nanoindentation testing of bone. Mechanical testing of bone and the bone implant interface. CRC Press, Boca Raton, FL, p. 257–269.

Rho, J.Y., Tsui, T.Y., Pharr, G.M., 1997. Elastic properties of human cortical and trabecular lamellar bone measured by nanoindentation. Biomaterials 8, 1325–1330.

Rho, J.Y., Zioupos, P., Currey, J.D., Pharr, G.M., 1999. Variations in the individual thick lamellar properties within osteons by nanoindentation. Bone 25, 295–300.

Rho, J.Y., Zioupos, P., Currey, J.D., Pharr, G.M., 2002. Microstructural elasticity and regional heterogeneity in human femoral bone of various ages examined by nano-indentation. Journal of Biomechanics 35, 189–198.

Sasaki, N., Odajima, S., 1996. Elongation mechanism of collagen fibrils and force–strain relations of tendon at each level of structural hierarchy. Journal of Biomechanics 29, 1131–1136.

Silva, M.J., Brodt, M.D., Fan, Z., Rho, J.-Y., 2004. Nanoindentation and whole-bone bending estimates of material properties in bones from the senescence accelerated mouse SAMP6. Journal of Biomechanics 37, 1639–1646.

Skedros, J.G., Bloebaum, R.D., Bachus, K.N., Boyde, T.M., 1993a. The meaning of graylevels in backscattered electron images of bone. Journal of Biomedical Materials Research 27, 47–56.

Skedros, J.G., Bloebaum, R.D., Bachus, K.N., Boyce, T.M., Constantz, B., 1993b. Influence of mineral content and composition on graylevels in backscattered electron images of bone. Journal of Biomedical Materials Research 27, 57–64.

Tai, K., Qi, H.J., Ortiz, C., 2005. Effect of mineral content on the nanoindentation properties and nanoscale deformation mechanisms of bovine tibial cortical bone. Journal of Materials Science—Materials in Medicine 16, 947–959.

Tarnowski, C.P., Ignelzi, M.A., Morris, M.D., 2002. Mineralization by developing mouse calvaria as revealed by Raman microspectroscopy. Journal of Bone and Mineral Research 17, 1118–1126.

Thompson, J.B., Kindt, J.H., Drake, B., Hansma, H.G., Morse, D.E., Hansma, P.K., 2001. Bone indentation recovery time correlates with bond reforming time. Nature 414, 773–776.

Vaidya, S.N., Karunakaran, C., Pande, B.M., Gupta, N.M., Iyer, R.K., Karweer, S.B., 1997. Pressure-induced crystalline to amorphous transition in hydroxylapatite. Journal of Materials Science 32, 3213–3217.

Wachtel, E., Weiner, S., 1994. Small-angle X-ray scattering study of dispersed crystals from bone and tendon. Journal of Bone and Mineral Research 9, 1651–1655.

Wang, X., Li, X., Bank, R.A., Agrawal, C.M., 2002. Effects of collagen unwinding and cleavage on the mechanical integrity of the collagen network in bone. Calcified Tissue International 71, 186–192.

Xu, J., Rho, J.Y., Mishra, S.R., Fan, Z., 2003. Atomic force microscopy and nanoindentation characterization of human lamellar bone prepared by microtome sectioning and mechanical polishing technique. Journal of Biomedical Materials Research Part A 67A, 719–726.

Yamashita, J., Li, X., Furman, B.R., Ralph Rawls, H., Wang, X., Agrawal, C.M., 2002. Collagen and bone viscoelasticity: a dynamic mechanical analysis. Journal of Biomedical Materials Research Part B 63, 31–36.